

Model-Based Respiratory Motion Compensation for Image-Guided Cardiac Interventions

Matthias Schneider^a, Hari Sundar^b, Rui Liao^b, Joachim Hornegger^a, and Chenyang Xu^b

^a Pattern Recognition Lab, University of Erlangen-Nuremberg, Erlangen, Germany

^b Siemens Corporate Research, 755 College Road East, Princeton, NJ 08540, USA

Abstract

In this paper we propose and validate a PCA-based respiratory motion model for motion compensation during image-guided cardiac interventions. In a preparatory training phase, a preoperative 3-D segmentation of the coronary arteries is automatically registered with a cardiac gated biplane cineangiogram, and used to build a respiratory motion model. This motion model is subsequently used as a prior within the intraoperative registration process for motion compensation to restrict the search space. Our hypothesis is that the use of this model-constrained registration increases the robustness and registration accuracy, especially for weak data constraints such as low signal-to-noise ratio, the lack of contrast information, or an intraoperative monoplane setting. This allows for reducing radiation exposure without compromising on registration accuracy. Synthetic data as well as phantom and clinical datasets have been used to validate the model-based registration in terms of registration accuracy, robustness and speed. We were able to significantly accelerate the intraoperative registration with a 3-D TRE of less than 2 mm for both monoplane images and intraprocedure settings with missing contrast information based on 2-D guidewire tracking, which makes it feasible for motion correction in clinical procedures.

1. Introduction

Minimally invasive cardiac interventions such as balloon angioplasty and coronary stenting for percutaneous re-canulation are routinely guided under X-ray fluoroscopy. Guidewire crossing of chronic total occlusions (CTO) within percutaneous coronary interventions (PCI) is challenging, in particular, due to the lack of blood flow and contrast concentration in the occluded segment resulting in poor X-ray guidance. The operator steers and advances the interventional instruments essentially blindly in the diseased artery. For this reason, highly experienced cardiologists are required to reduce the high risk of hemorrhage, perforation or even dissection of the artery wall.

Integrating preoperative plans into the interventional surgery suite is a common way to assist the surgeon during the intervention. In the case of PCI for CTO, computed tomography (CT) guidance is able to provide useful visual information. A 3-D segmentation of the coronary tree can be reconstructed from a preoperative cardiac CT [3] and then be overlaid on top of the intraoperative 2-D fluoroscopy [14]. In this way, the surgeon is provided with additional visual information about the position of the vessel branches and the occlusion. However, maintaining up-to-date information during the intervention requires continuous re-adjustment of the registration due to cardiac and respiratory motion. Such *re-registrations* of preoperative volumetric datasets with intraoperative images are challenging and computationally demanding due to the low quality and lack of contrast in intraprocedure fluoroscopic images.

Related Work Various techniques have been proposed to overcome the problem of cardiac and respiratory motion in cardiac imaging. Errors due to cardiac motion can partly be avoided using electrocardiography (ECG) gating. Since the human heart rate is usually no smaller than 60 beats per minute, ECG gating results in a frame rate of about one frame per second. Similar approaches for respiratory gating in cardiac magnetic resonance imaging (MRI) have been investigated, usually using displacement transducers to estimate the breathing phase [1]. Due to the relatively long breathing cycle of several seconds, the resulting imaging frequency of respiratory-gated angiograms is significantly reduced and is not practical for interventional applications. Another strategy for reducing respiratory motion is the breath-hold technique [9]. Even if this method successfully reduces breathing motion by simple and natural means, it is significantly restricted by the patient's limited ability to perform a supervised breath-hold during the treatment or image acquisition [5]. A third class of strategies copes with the problem of respiratory motion correction by incorporating suitable motion models. Manke *et al.* [7] proposed a patient-specific affine motion model based on a diaphragmatic pencil-beam navigator for prospective respiratory motion correction in coronary MRI. In a follow-

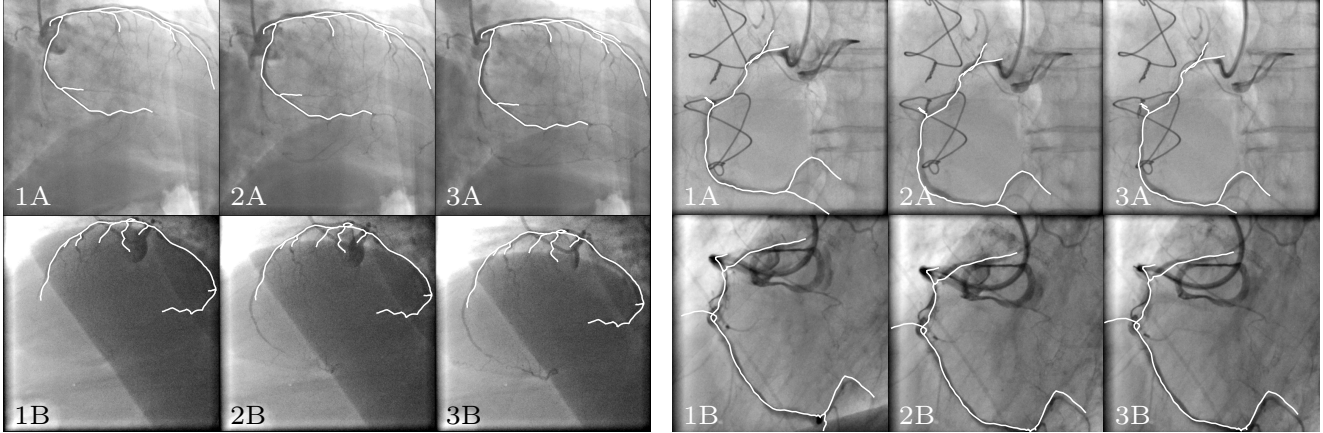


Figure 1: First three samples of the ECG-gated biplane angiogram of two clinical cases with registered preoperative coronary centerline. The registration results are used as training samples for the estimation of the patient-specific motion model.

up study [6] the authors extended the technique by multiple transducers at moving structures to achieve better correlation particularly for non-translational components of the affine parameter set. Similarly, King *et al.* [4] proposed a motion model for respiratory motion correction of MRI-derived roadmaps for use in X-ray guided cardiac catheterization procedures. The model uses second order polynomials to relate the diaphragmatic position to the affine pose parameters. The intraprocedure diaphragm tracking requires manual landmark selection and relies on the diaphragm to be visible in the images. The authors report a model accuracy of 2–4 mm in 3-D and 3–4 mm in 2-D, respectively. In another series of studies, an algorithm employing a parametric 3-D+time coronary model [11] is developed to correct X-ray images for both cardiac and respiratory motion [13]. The diaphragm tracking again requires manual landmark selection. Another major drawback of the proposed navigator-based techniques is that they purely rely on the transducer data to “predict” the corresponding pose parameters without considering any further image information. Therefore, intra-subject variabilities within the breathing cycle can not be accounted for.

Studies on respiratory motion of the heart [8, 12] have concluded that breathing motion can be approximated as rigid transformations with a patient-specific profile. Even though this kind of motion is more complex than just pure 3-D translation, the profile is restricted in terms of both 3-D rotation and translation. In this paper, we learn this patient-specific motion, by applying Principal Component Analysis (PCA) on samples obtained from rigid 2-D/3-D registration [14] of a preoperative 3-D segmentation of the coronary arteries [3]. The PCA model is subsequently used to constrain re-registrations performed during interventions. The use of this patient-specific model as prior knowledge greatly improves the re-registration accuracy and robustness even

when performed using a monoplane image or fluoroscopic images without contrast. It is also superior in terms of computation time compared to the unconstrained registration.

2. Methods

The basis for our respiratory motion analysis are 2-D biplane angiograms. Applying ECG gating extracts a sequence of X-ray images showing the contrast-enhanced coronary arteries at a fixed cardiac phase, thereby isolating the respiration induced motion which is assumed to be rigid.

To estimate the pose of the vasculature in each image, we applied a feature-based 2-D/3-D registration algorithm [14] optimizing for a rigid transformation that best maps a pre-operative 3-D centerline segmentation of the coronary arteries to the 2-D biplane angiograms. The coronary centerline has been reconstructed from segmented preoperative 3-D CT datasets [3] at the same gated cardiac phase. In the following sections, we describe how the model is built and leveraged to augment and accelerate the unconstrained registration framework.

2.1. Motion Model

According to previous studies, respiratory motion of the heart shows a restricted profile [8, 12]. To capture and mathematically describe these patient-specific restrictions, we analyzed the pose of the coronaries at different breathing phases. For this purpose, the coronary segmentation was registered with a sequence of N ECG-gated angiograms at different respiratory phases (see Figure 1). For each captured breathing phase, we obtain an estimate for the corresponding cardiac pose which is represented by a rigid transform $\mathbf{m}_i \in \mathbb{R}^6 (1 \leq i \leq N)$. We assume \mathbf{m}_i to form a linear (low-dimensional) sub-manifold embedded in the six dimensional space of rigid 3-D transformations. Lin-

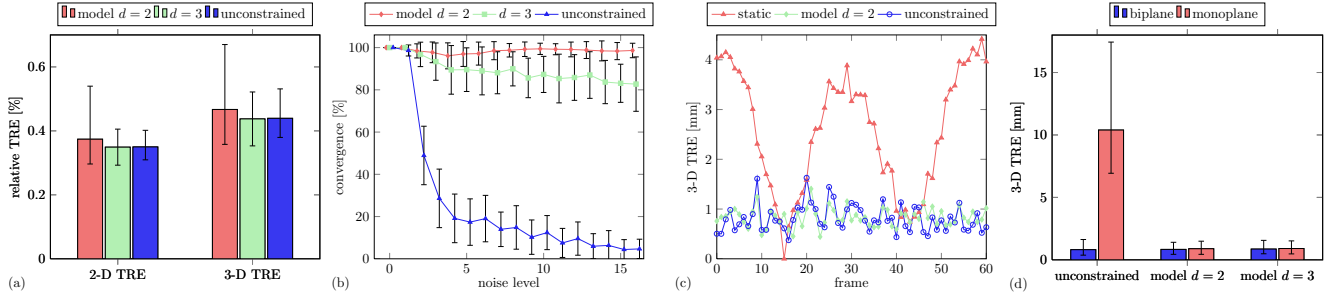


Figure 2: *Synthetic Data*: (a) Mean relative 2-D/3-D TRE of the model-constrained registration with model dimension $d = 2$ and $d = 3$ compared to the unconstrained optimization using a manually reconstructed coronary tree from CT data. Error bars show the minimum and maximum relative TRE. (b) Mean ratio of converged solutions for initial guesses at different noise levels. A threshold of 2% for the mean 3-D TRE was used as convergence criterion. Error bars indicate the standard deviation. *Phantom Experiments*: (c) 3-D TRE over entire breathing cycle for static and motion-compensated overlay using the unconstrained and model-based approach for $d = 2$. The motion model was trained on $N = 7$ samples. (d) Mean 3-D TRE of phantom validation for mono and biplane setting. Error bars visualize the minimum and maximum TRE.

ear PCA is applied to find the corresponding basis vectors. Singular value decomposition [10] is used to compute the eigenvalues $\lambda_1 \geq \dots \geq \lambda_6$ and corresponding eigenvectors $\mathbf{v}_1, \dots, \mathbf{v}_6$ of the covariance matrix Σ . The basis of the d -dimensional linear sub-manifold ($d \leq 6$) is then identified as the first d eigenvectors corresponding to the d largest eigenvalues $\lambda_1, \dots, \lambda_d$. The spectrum of Σ can be used to define a proper value for the dimension d . We eventually obtain the d -dimensional linear motion model \mathcal{M}^d which captures the patient-specific respiratory profile:

$$\begin{aligned} \mathcal{M}^d : \mathbb{R}^d &\rightarrow \mathbb{R}^6 \\ \boldsymbol{\alpha} &\mapsto \bar{\mathbf{m}} + \sum_{i=1}^d \alpha_i \mathbf{v}_i \end{aligned}, \quad (1)$$

where $\bar{\mathbf{m}}$ is the mean transform $\bar{\mathbf{m}} = \frac{1}{N} \sum_{i=1}^N \mathbf{m}_i$. For the rotation parameterization we are using the three Euler angles. Since this kind of representation has many known drawbacks such as ambiguities and singularities, we also experimented with the exponential map parameterization [2]. Despite the advantages of the exponential map over Euler angles, we could not find any remarkable differences between the parameterizations in terms of model accuracy. Due to the different units and magnitudes, it is beneficial to normalize the training data before “mixing up” rather dominant translation with much smaller rotation components. For this reason, each component is scaled by the inverse of the component-wise variance before applying PCA. Strictly speaking, this equals to decomposing the *correlation matrix* of the input data to obtain the principal axes \mathbf{v}_i .

For the model estimation, an initial sequence of biplane X-ray angiograms has to be acquired prior to the intervention. Alternatively, two monoplane sequences from different angulations can be used just as well. A free-breathing protocol ensures sufficient training samples populating the entire respiratory cycle.

2.2. Model-Constrained Registration

The estimated motion model provides a low-dimensional parameterization that spans the space of valid configurations within the breathing cycle. Therefore, the patient-specific model can be used as prior to restrict the search space during *re-registrations*. The algorithm no longer optimizes for the six parameters describing an arbitrary rigid transform but only for $d \leq 6$ model parameters $\boldsymbol{\alpha}$, the principal components, to estimate the pose parameters:

$$\hat{\mathbf{m}} = \mathcal{M}^d \left(\arg \min_{\boldsymbol{\alpha} \in \mathbb{R}^d} \sum_{k=1}^2 C_k(I_k, \Upsilon_0, \mathcal{M}^d(\boldsymbol{\alpha})) \right), \quad (2)$$

where $C_k(I, \Upsilon_0, \mathbf{m})$ is a similarity measure based on a modified Euclidean distance transform [14]. It describes the average distance between the angiogram I of camera k and the preoperative 3-D centerline segmentation Υ_0 which is transformed according to the rigid mapping \mathbf{m} and projected into the camera coordinate frame. I_1 and I_2 denote two corresponding camera images of the biplane system. For a monoplane setting C_2 is set to zero. We want to point out that the utilization of the motion model is not limited to the particular 2-D/3-D registration and similarity measure proposed in [14] but it can be leveraged in any other registration framework, too.

Live fluoro images for X-ray guidance during PCI for CTO are usually acquired without contrast due to the occlusion and the limited expected benefit. Therefore, most of the structural information is missing, which makes the registration problem ill-posed and challenging. The guiding catheter and guidewire (GW) provide the only indication for the hidden coronary arteries. The registration workflow is similar to the angiography case with contrast but incorporates 2-D GW tracking [15] combined with a similarity measure using the mean point-wise difference of the tracked

	S1 N=95	S2 N=133	S3 N=110	S4 N=217	P1 N=7	C1 N=5	C2 N=6
λ_1	4.9321	4.9299	5.3875	5.1747	3.3129	2.9595	4.8727
λ_2	0.8780	0.9217	0.4820	0.6453	1.7693	2.4978	0.7244
λ_3	0.1416	0.1317	0.0980	0.1160	0.6827	0.5315	0.3941
λ_4	0.0396	0.0144	0.0299	0.0409	0.1970	0.0212	0.0088
λ_5	0.0067	0.0014	0.0021	0.0207	0.0381	0.0000	0.0001
λ_6	0.0020	0.0009	0.0006	0.0024	0.0000	0.0000	0.0000

Table 1: Model spectra of (S)ynthetic, (P)antom, and (C)linical data sets. The eigenvalues λ_k of the correlation matrix are sorted in descending order.

GW and the projected 3-D segmentation to assess the quality of the considered overlay. Strictly speaking, we consider only a subset of the 3-D segmentation in this case. It describes a roadmap of the planned GW path defined by the location of the CTO. This information is available from the planning prior to the procedure. The optimization process uses one additional parameter as offset in the preselected roadmap to compute the mean point-wise distance to the tracked GW.

3. Validation and Experimental Results

Both synthetic and clinical data have been used for the validation of our proposed model-constrained registration algorithm.

Synthetic Data: A respiratory motion generator was implemented based on a clinical study on human breathing motion providing pose samples of tracked displacement transducers attached to the chest of four subjects [16]. The covariance matrices of these four sample sets share a sharp spectrum with a prominent first eigenvalue as listed in Table 1. The corresponding eigenvector describes mostly inferior-superior translation. The motion model estimation within the simulation was based on $N = 8$ random samples and validated for another 32 random samples per motion generator. For the arterial 3-D centerline segmentation Υ_0 , we used both a set of uniformly distributed 3-D points and a manually segmented CT dataset and added Gaussian noise to account for inevitable reconstruction errors in a clinical setting. The intraoperative biplane angiograms were obtained by transforming the 3-D segmentation by a random sample of the motion generator, adding Gaussian noise, and projecting this imaginary 3-D observation on two cameras.

To assess the benefits of our model-based approach, we compared it to the unconstrained registration in terms of accuracy, robustness and speed. The simulation uses a Nelder-Mead Simplex optimizer with the model’s mean transform \bar{m} as initial guess for both the model-constrained and the unconstrained registration. The experiments on phantom and clinical data employ an adaptive best-neighbor optimizing scheme for better robustness of the unconstrained registration, in particular. Concerning registration accuracy, we considered the 2-D and 3-D target-to-registration error

(TRE). The latter computes the average spatial distance between the 3-D ground truth (target) and the registered segmentation Υ_0 with the mean L_2 -norm of the point-wise difference vectors as distance metric. The 2-D TRE was computed correspondingly after projecting to the camera space. It is a measure for the perceived error when looking at the angiograms, whereas the 3-D TRE better reflects the true 3-D mismatch. Since the experimental respiratory motion data are given in relative coordinates, we report relative error measures that are obtained from the absolute TRE divided by the maximum side length of the bounding box in 2-D and 3-D, respectively. Both 2-D and 3-D TRE show the same pattern illustrated in Figure 2a. Even if the model-constrained approach for model dimension $d = 2$ results in a slightly larger TRE compared to the unconstrained approach, the differences become marginal for $d = 3$.

There is a remarkable difference in terms of speed, though, which was benchmarked based on the average number of cost function evaluations. For the simulation, the number of iterations decreased from 194 ± 25 for the unconstrained approach to 78 ± 9.1 for $d = 3$ and 50 ± 5.8 for $d = 2$, respectively. The number of cost function evaluations for the unconstrained case is still moderate due to the good initialization.

Finally, we analyzed the capture range to compare the robustness. The registration was initialized with different initial guesses with subsequently added Gaussian noise starting from the optimal initial guess closest to the random sample of the motion generator. Figure 2b confirms that the utilization of prior information on breathing motion within the registration process results in much better robustness, whereas the full-space optimization fails to converge to a reasonable solution even for small noise levels.

Phantom Experiments: A second set of experiments was carried out on a biplane C-arm system (AXIOM Artis, Siemens Medical Solutions, Erlangen, Germany). We acquired fluoroscopic image sequences of a sophisticated cardiac phantom which is capable of simulating cardiac and respiratory motion. As illustrated in Figure 3, the phantom consists of a fluid-filled balloon (heart) surrounded by small tubes (coronary arteries). An external pump periodically inflates and deflates the tubed balloon (cardiac motion) which is mounted on a ramp that changes its incline periodically (respiratory motion). The 3-D centerline Υ_0 has been reconstructed from a CT of the phantom. For the initial motion model estimation we acquired a biplane sequence of the phantom with simulated cardiac and respiratory motion. After applying ECG gating, and initial registration, this data provided 7 samples at different breathing phases which served as training data for the motion model, see Figure 3. The estimated model was then validated using a second biplane sequence of 61 images with shallow breathing covering a whole breathing cycle with cardiac motion dis-

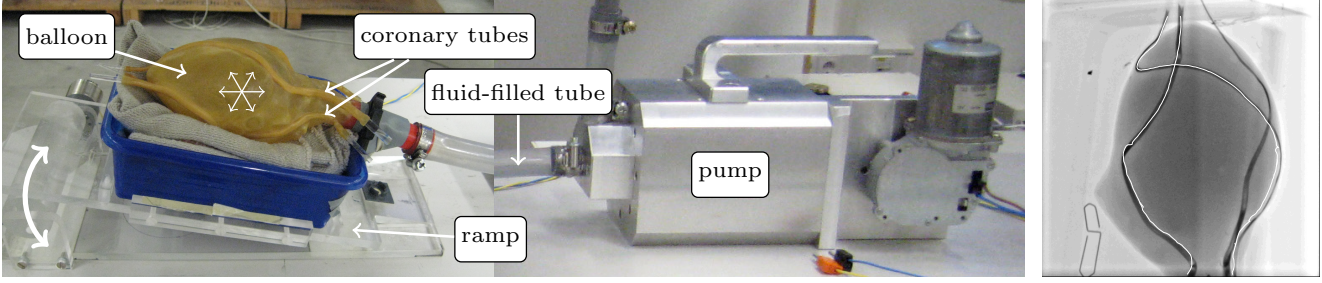


Figure 3: Left: Cardiac phantom installation with simulation mechanism for cardiac and respiratory motion. The pump periodically inflates and deflates the fluid-filled balloon mounted on a ramp which is mechanically lifted and lowered. Right: X-Ray image of the cardiac phantom with registered coronary centerline.

abled. The unconstrained biplane registration was used to generate the ground-truth (target) with manual refinement whenever necessary. Figure 2c illustrates the mean 3-D TRE over the breathing cycle for a static overlay and the model-based motion correction. The ground-truth solution of the frame in the middle of deep in- and exhale phase was chosen as static overlay. Consequently, the 3D TRE peaks at the extreme breathing phases with an amplitude of about 4 mm. The model-based motion compensation is able to permanently reduce the error to 0.84 ± 0.19 mm and 2.0 ± 0.53 px, respectively.

One of the major advantages of the model-based registration appears for intraoperative **monoplane** settings. In this case, the biplane information is used for the initial model estimation only. The subsequent re-registrations, however, make use of only one of the two sequences. Even when the unconstrained registration matches the considered monoplane almost perfectly (small 2-D TRE), it shows a significant mismatch for the unconsidered view. This discrepancy is reflected in the resulting average 3-D TRE shown in Figure 2d. The model-based registration approach turns out to be superior and much more robust in this case. The underlying model reasonably restricts the search space so that the registration still converges to a reasonable solution. In terms of speed, we were able to reduce the number of cost function evaluations for the biplane case from 630 ± 93 iterations to 56 ± 13 ($d = 3$) and 34 ± 6.1 ($d = 2$), respectively. For the monoplane comparison, we get a similar pattern. Because of its small capture range, the unconstrained registration is implemented as two-stage best-neighbor optimization at a coarse and fine scale, which increases the number of cost function evaluations but showed best robustness and results in this case.

Clinical Experiments: We repeated the above experiments on patient data obtained from coronary intervention cases. Most of the cineangiograms being acquired during clinical interventions are relatively short to minimize dose and contrast agent, which hampers the reliable motion model estimation and validation. We present prelimi-

nary results on two clinical cases with preoperative biplane cineangiograms providing five (case 1) and six (case 2) gated samples at different breathing phases, see Figure 1. The motion model is trained on these samples and captures a complex motion profile that describes the characteristics of the patient-specific respiratory motion (see Figure 4a). We used a leave-out-one strategy to train the motion model on all but one samples and validated for the one left out. The registration accuracy of both cases is summarized in Figures 4b-4c for the mono- and biplane setting. The average 3-D TRE shows the same pattern as for the phantom experiments. For the model-constrained biplane scenario, it is in the range of 1–1.5 mm and slightly increases for the monoplane setting, whereas the unconstrained approach yields an incorrect registration. The CT nicely aligns with the considered monoplane image but shows a remarkable offset in the unconsidered view. Even though the first major modes are dominated by inferior-superior translation, the captured motion profile also describes the rotational part and hence performs better than the unconstrained registration optimizing for pure 3-D translation with constant rotation of the mean transform \bar{m} .

Incorporating the motion model as prior into the registration framework allows to not only reduce the search space and hence accelerate the overall registration process but also provides a better parameterization of the search space that better fits the input data. The re-parameterization has a crucial effect on the shape of the cost function as illustrated in Figure 5. The cost function shows a much smoother profile for the model parameterization, suggesting that the constrained optimization problem is well-posed, as opposed to the unconstrained optimization with conspicuous local extrema, indicating that the problem is, at-least, ill-conditioned. The smooth profile allows for sophisticated optimization strategies, e.g., conjugate gradient method, incorporating gradient information resulting in even faster convergence in average without compromising on robustness and registration accuracy.

Finally, we assessed the accuracy for intraprocedure re-

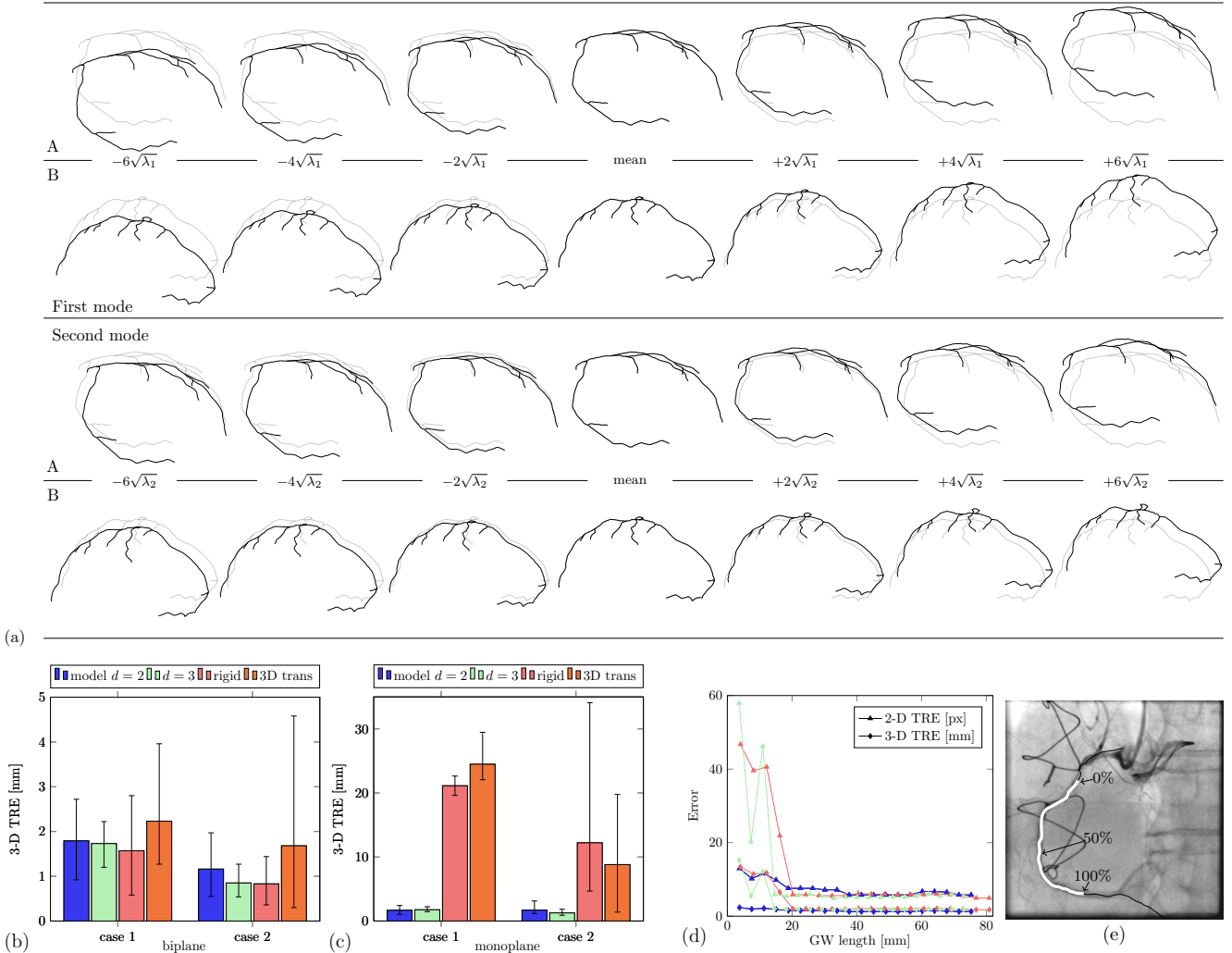


Figure 4: (a) Visualization of the respiratory motion profile captured by the first and second major mode in the range of $\pm 6\sqrt{\lambda_{1,2}}$ for the first clinical case. The mean transform \bar{m} is shown in light gray. (b,c) 3-D TRE of model-based and unconstrained registration using rigid transformation and 3-D translation, respectively, to model respiratory motion in both clinical cases for (b) biplane and (c) monoplane scenario. Error bars indicate the minimum and maximum error. (d) Registration accuracy for different guidewire (GW) simulations (color-encoded) based on both clinical datasets for varying guidewire segments and lengths. (e) Angiogram of clinical case 2 with the registered GW roadmap (subset of CT segmentation). The highlighted segment (white) has a total length of 75.3 mm in 3-D and was used for the GW simulation in this case.

registrations based on 2-D GW tracking. Since quantitative validation is not meaningful due to the lack of contrast, we simulated the GW in 2-D based on the gold standard registration of the angiographies with contrast. A manually selected segment of the projected CT segmentation with added Gaussian noise was considered the tracked GW, see Figure 4e. The model-based registration of the CT with the simulated GW was then compared to the ground-truth of the underlying angiogram. The resulting 2-D/3-D TRE are shown in Figure 4d for varying GW lengths. The error declines with increasing GW length and reaches almost the same level of accuracy as the contrast-based regis-

tration. The unconstrained registration totally fails for this ill-conditioned missing information problem.

4. Conclusions

In the first set of experiments, we validated our model-based registration for synthetic data. Leveraging the motion model as prior in the registration framework to re-parameterize and reasonably restrict the search space, makes the numerical optimization more robust and faster without compromising on registration accuracy. The prospective use of the model-constrained registration was

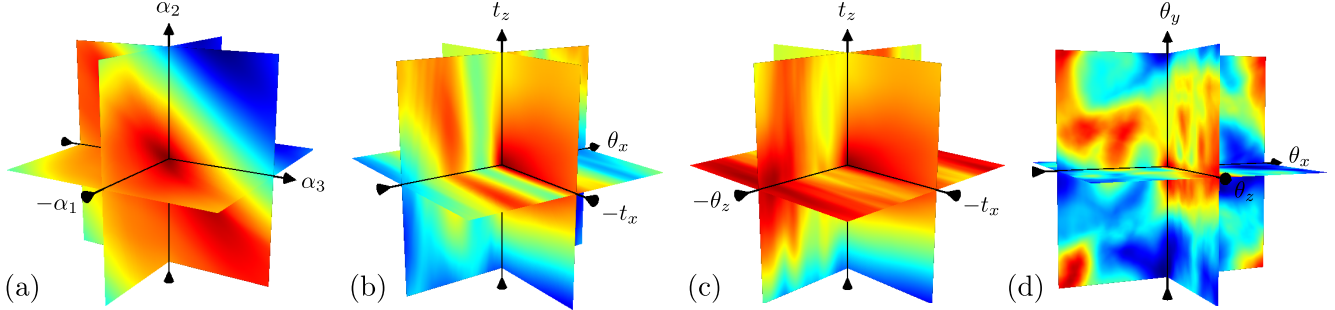


Figure 5: Normalized cost function evaluated in the proximity of the gold standard (origins) for (a) varying model parameters $\alpha_{1,2,3}$ in the range of $\pm 16\sqrt{\lambda_{1,2,3}}$ and (b-d) different combinations of translation $t_{x,y,z}$ and rotations $\theta_{x,y,z}$.

tested in the second set of experiments using phantom and clinical data. We have shown that a low-dimensional model is able to capture the respiratory motion profile and has a smoothing effect on the cost function. A registration accuracy of less than 2 mm was achieved even for intraoperative settings with monoplane image data or missing contrast information.

Although the patient will be exposed to additional radiation and contrast agent during the initial training phase, the reduction from the availability of breathing compensated overlay and the possible use of monoplane images for guidance should greatly reduce the overall radiation exposure for the procedure.

References

- [1] R. L. Ehman, M. T. McNamara, M. Pallack, H. Hricak, and C. B. Higgins. Magnetic resonance imaging with respiratory gating: techniques and advantages. *American Journal of Roentgenology*, 143(6):1175–1182, December 1984.
- [2] F. S. Grassia. Practical parameterization of rotations using the exponential map. *Journal of Graphics Tools*, 3(3):29–48, March 1998.
- [3] M. A. Gülsün and H. Tek. Robust vessel tree modeling. In *Medical Image Computing and Computer-Assisted Intervention – MICCAI 2008*, volume 5241 of *LNCS*, pages 602–611. Springer, 2008.
- [4] A. King, R. Bouberkakh, K. Rhode, Y. Ma, P. Chinchapattanam, G. Gao, T. Tangcharoen, M. Ginks, M. Cooklin, J. Gill, D. Hawkes, R. Razavi, and T. Schaeffter. A subject-specific technique for respiratory motion correction in image-guided cardiac catheterisation procedures. *Medical Image Analysis*, 13(3):419–431, June 2009.
- [5] G. S. Mageras and E. Yorke. Deep inspiration breath hold and respiratory gating strategies for reducing organ motion in radiation treatment. *Seminars in Radiation Oncology*, 14(1):65–75, January 2004.
- [6] D. Manke, K. Nehrke, and P. Börnert. Novel prospective respiratory motion correction approach for free-breathing coronary MR angiography using a patient-adapted affine motion model. *Magnetic Resonance in Medicine*, 50(1):122–31, July 2003.
- [7] D. Manke, K. Nehrke, P. Börnert, P. Rösch, and O. Dössel. Respiratory motion in coronary magnetic resonance angiography: A comparison of different motion models. *Journal of Magnetic Resonance Imaging*, 15(6):661–671, May 2002.
- [8] K. McLeish, D. Hill, D. Atkinson, J. Blackall, and R. Razavi. A study of the motion and deformation of the heart due to respiration. *IEEE Transactions on Medical Imaging*, 21(9):1142–1150, September 2002.
- [9] M. R. Paling and J. R. Brookeman. Respiration artifacts in MR imaging: reduction by breath holding. *Journal of Computer Assisted Tomography*, 10(6):1080–1082, November 1986.
- [10] W. Press, S. Teukolsky, W. Vetterling, and B. Flannery. *Numerical Recipes in C*. Cambridge University Press, Cambridge, UK, 2nd edition, 1992.
- [11] G. Shechter, C. Ozturk, J. R. Resar, and E. R. McVeigh. Respiratory motion of the heart from free breathing coronary angiograms. *IEEE Transactions on Medical Imaging*, 23(8):1046–1056, August 2004.
- [12] G. Shechter, J. Resar, and E. McVeigh. Displacement and velocity of the coronary arteries: cardiac and respiratory motion. *IEEE Transactions on Medical Imaging*, 25(3):369–375, March 2006.
- [13] G. Shechter, B. Shechter, J. Resar, and R. Beyar. Prospective motion correction of X-ray images for coronary interventions. *IEEE Transactions on Medical Imaging*, 24(4):441–450, April 2005.
- [14] H. Sundar, A. Khamene, C. Xu, F. Sauer, and C. Davatzikos. A novel 2D-3D registration algorithm for aligning fluoroscopic images with pre-operative 3D images. In *Proceedings of SPIE*, volume 6141, San Diego, CA, USA, February 2006.
- [15] P. Wang, T. Chen, Y. Zhu, W. Zhang, S. K. Zhou, and D. Comaniciu. Robust guidewire tracking in fluoroscopy. In *IEEE International Conference on Computer Vision and Pattern Recognition*, 2009.
- [16] W. Wein, J.-Z. Cheng, and A. Khamene. Ultrasound based respiratory motion compensation in the abdomen. In *MICCAI 2008 Workshop on Image Guidance and Computer Assistance for Soft-Tissue Interventions*, September 2008.